Summary

The design of airplanes is an analytical and iterative process, involving the analysis of functions of the various subsystems and the requirements they must fulfill. There are multiple constraints on the design, ranging from the cost of production to efficiency of operation.

This report aims to present the process of designing the structure of a small business jet. The procedure first included the derivation of an initial propulsion system design and other elements to conclude a class II weight estimation. The previously determined aircraft components were utilized, along with other components found in previous work packages, to make a class II zero-lift drag estimation. Given the interdependence between the class II weight estimation and the class II drag estimation of the aircraft, a design loop was encountered. This loop was managed through an iterative Python process to identify the converged final aircraft weight.

Contents

List of Tables

List of Figures

List of Symbols

Symbol	Definition	S.I. Unit

1

Introduction

Understanding the behaviour of an airfoil lies at the base of all aircraft performance and is therefore of the utmost importance. Since people learned how to make aircraft, wind tunnels have been used to analyse the performance of different airfoils, and they are still irreplaceable pieces of technology to this day. Modern technology has also provided us with the possibility of analyzing airfoil performance numerically using computer programs. This report aims to analyse the behaviour of a SD6060 airfoil both experimentally and numerically, and provide insight on the difference in results between the two methods.

The experiment will be conducted at the TU Delft Small Low Turbulence wind tunnel (SLT) of the Faculty of Aerospace Engineering. Two tests will be conducted: one using a finite wing setup using a wing including a wingtip, and one using an infinite wing setup with an extended airfoil set between two flat plates. After this experiment has been conducted, the same airfoil will be analysed using aerodynamic analysis software such as XFOIL and XFLR5. Lastly, the results of these analyses will be compared to find and explain the differences between the two methods of analysis.

The report is structured as follows: In chapter 2 the methodology used in the experiment will be described, of which the results will be analysed in chapter 3. Following this, the results of the numerical analysis will be presented and compared to the experimental results in chapter 4. Lastl,y the discussion of the report will be given in chapter 5.

2

Methodology

This chapter will aim to provide a complete description of the wind tunnel, along with an explanation on the different test models that were utilized for the 2D and 3D experiments. In addition, the techniques for measuring pressure and force will be shared, along with a flow visualization technique. Lastly, some light will be shed on the reference speed of the wind tunnel, the different corrections that must be made due to the presence of the tunnel, and the numerical tools and methods used for simulating the experiment.

2.1. Wind Tunnel
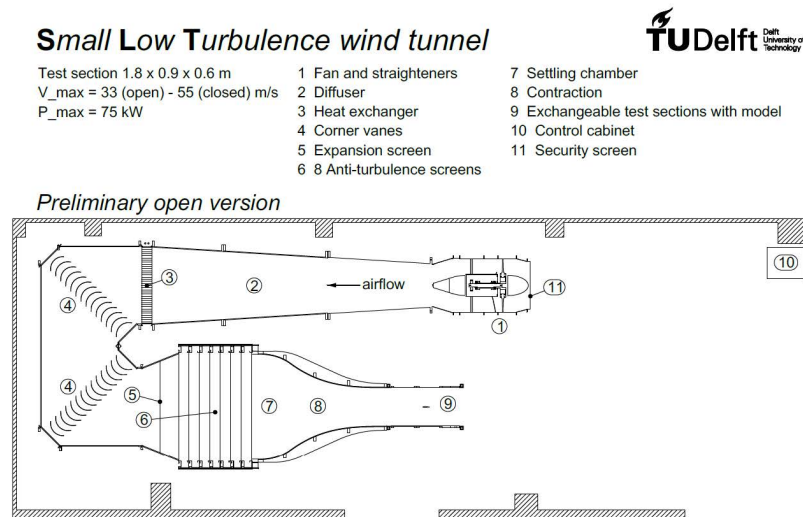
Figure 2.1: The Small Low Turbulence (SLT) Wind Tunnel layout

The measurements were performed in the Small Low Turbulence (SLT) wind tunnel facility at the Delft University of Technology. The SLT wind tunnel provides the opportunity to test the aerodynamics properties of airfoils and wings by providing a smooth laminar flow of air. The wind tunnel was set up in the open-loop configuration, which is comprised of the following sections:

- A Fan with straighteners that generates the airflow
- A Diffuser section which decelerates the airflow and thus increases the static pressure, which reduces turbulence
- A heat exchanger for controlling the temperature of the air coming from the diffuser
- Corner vanes which guide the flow around 90 degree angles, preventing flow separation.
- The settling chamber, which starts with an expansion screen, followed by eight anti-turbulence screens. The air leaving this chamber is laminar and steady
- Contraction compartment which speeds up the laminar flow with a contraction ratio of 11:1
- Exchangeable test section which where the models are placed and the measurements are taken.

2.2. 3D and 2D models

To measure key wing and airfoil properties, a scaled down model must be used that allows for turning on and off 3D wing characteristics, such as tip vortices, while also allowing for a tuneable α
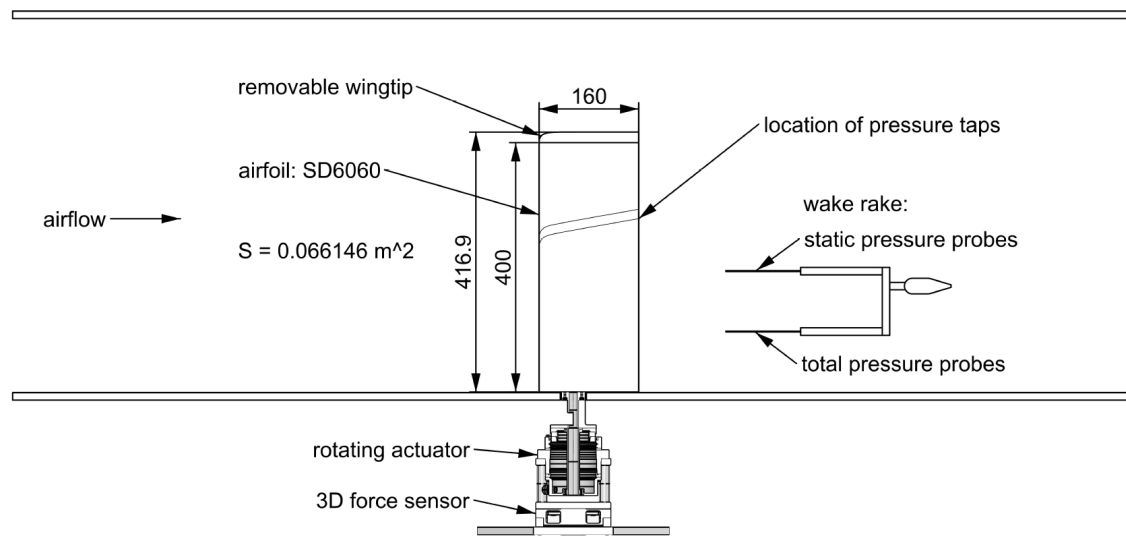
Figure 2.2: Drawing of 3D model

The model and setup used for measuring 3D wing characteristics is shown in figure 2.2, including its dimensions. A straight wing with a detachable rounded tip was used. The cross-section of the wing is modeled after the SD6060 airfoil. Along the top and bottom of the wing, along the chordwise direction, small punctures were made which serve as pressure taps. These taps are distributed along the span of the wing to make sure they do not interfere with each other. The wing is mounted on a reflective turntable, to which a force balance is also attached capable of measuring lift, drag, and pitching moment (see section 2.3). The turntable allows for a variable α.
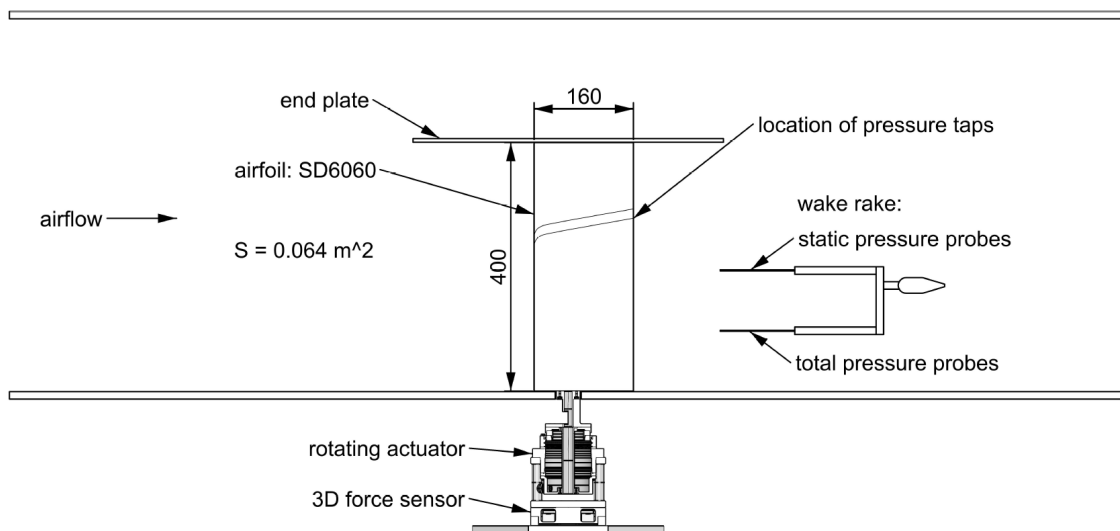
Figure 2.3: Drawing of 2D model

To emulate a 2D environment, the tip of the wing is removed and replaced with an end plate as shown in figure 2.3. This removes the effect of tip vortices, turning the setup into a quasi-2D model. Instead of a force balance, a wake rake is now added for determining the total drag (section...)

2.3. Measurement Techniques

Pressure Taps
To find the pressure distribution along the airfoil, we can use pressure taps. Pressure taps are small openings located on the surface of the wing. The taps enable pressure measurements at the surface. They are located along the span, so that they are not placed in a single line along the chord, as that could skew the measurements.

Wake Rake
To measure what is happening in the wake of the airfoil, we can use a wake rake, which is a collection of small pipes, placed in a line perpendicular to the span and the chords. There are two sets of pipes, one that measures the static pressure, and the other responsible for measuring the dynamic pressure. These pressure measurements can be tunred into a veloctiy profile at the wake.

insert wake rake figure

Force Balance
The force balance is used to find the drag and lift in the 3D case as using the wake rake for finding the lift and drag is strictly a 2D concept.

Tufts
Tufts are visual ques that help visualise the flow. They are small pieces of felt, attatched at various parts of the wing. Since the tufts move with the flow you can get an idea of whether the flow is turbulent or smooth and which direction it is going in.

2.4. Reference wind tunnel speed
In the section of the windtunnel right before the test section and after the settling chamber, pressure sensors are installed which can be used to measure the velocity of the flow. With an empty test section, pressure readings are done for different velocity settings, with which a lookup table can be made attaching each pressure value to a flow velocity. When the model is then put in the test section, the pressure reading can be used to find the corresponding reference wind tunnel velocity.

2.5. Wind tunnel Corrections
Wind tunnel corrections account for the fact that the model is tested not-ideal flow environment caused by the tunnel and the measurement instruments. These adjustments are applied to the measured data so it more accurately represents uniform, undisturbed flow. Three sources of disruptions are corrected for: model blockage, wake blockage, and lift interference.

Model blockage
Also known as solid blockage corrections is caused by the finite volume of the model which occupies part of the test-section cross-section. This causes a reduction in the cross-sectional area available for the flow to pass. According to the continuity formula for one-dimensional, inviscid, incompressible flow with no body forces, this decrease in cross-sectional area increases velocity near the model, which in turn leads to a change in pressure, as per Bernoulli's principle. This increase in velocity leads to an over-prediction of the aerodynamic forces if uncorrected.

Wake blockage
Wake blockage occurs due to the viscous effects in the wake region behind the test model. In the wake region, the flow has a decreased velocity compared to the freestream velocity, and to satisfy continuity, the velocity outside the wake region must increase. This artificially increases the local freestream velocity and decreases the pressure experienced by the model. Unlike model blockage, wake blockage is configuration-dependent, meaning that it varies with aerodynamic loading, and it increases rapidly with AoA and flow separation since it highly depends on Drag.

Lift interference

Lift interference correction accounts for the alteration of the lift-induced flow field due to the tunnel walls, which restricts the expansion fo the streamlines, modifying the downwash and pressure distribution associated with the generation of lift. The walls generate an upwash at the model, which increases the effective AoA and causes a systematic over-prediction of the C_L, lift-curve slope and pitching moment compared to their actual values in free-stream conditions. These effects become increasingly uncertain near stall and in separated flows.

2.6. Numerical Methods

In order to interpret our measured results we will create a model and simulations using numerical methods and compare our measured results to those. To create the model and simulations we will use the prgrammes XFOIl and XFLR5

XFOIL - 2D panel method

XFOIL is an interactive tool used to design and analyze subsonic 2D airfoils which uses a version of the vortex panel method for its calculations. When given an airfoils coordinate geometry along with Reynolds and Mach numbers, it can compute the pressure distribution and determine resulting lift and drag. The software can be used for relatively low Reynolds numbers. Since we know the coordinate geometry, all we have to do is specify the mach and Reynolds numbers which we can read in the wind tunnel.

XFLR5 - 3D methods

Since XFOIL is not capable of simulating 3D data, XFLR5 is used. While three-dimensional wings are simulated with similar methods as 2D airfoils, XFLR5 adjusts for the finite nature of the wing. Due to the difference in low and high pressure between the top and bottom sides of the wing, wingtip vortices and downwash are created at the tip of the wing. While the wingtip vortices induce drag, downwash reduces the effective angle of attack experienced by the wing.

To account for these effects, XFLR5 employs the following four different numerical methods according to XFLR5 Development Team [2]:

1. **LLT** - The "Lifiting Line Theory" replaces a lifting wing with a lifting line. With the basic linear assumption of $C_L = f(\alpha)$, results are then interpolated from non-linear sections of the curve with results from 2D data. While the LLT does not directly account for viscosity, the 2D viscous results introduce it indirectly, allowing for profile drag estimations. This method is suggested for wings with a high aspect ratio and low sweep.

2. **VLM1** - The more "classic Vortex Lattice Method" allows for the analysis of wings that cannot be accurately calculated by means of LLT. With a VLM, the vortices across the wing planform are calculated while considering the necessary boundary conditions. As a result, the disturbance produced by the wing is found. To do this, a horseshoe vortex is placed at the quarter chord of the panels. This method, however, only considers the wings' mean chord and fails to consider sideslip.

3. **VLM2** - The "alternative Vortex Lattice Method" works with the same principle as the classical one, but extends the trailing vortices to infinity. Results are however, nearly identical.

4. **3D Panel** - The "3D Panel Method" serves as an alternative to LLT and VLM that can take wing thickness, fuselage, and CP distribution on either side of the wing into account. It has a higher computational cost as it models perturbations by adding doublets and sources over all surfaces. This method is limited by the quality and accuracy of the mesh.

None of these methods is suitable to predict stall or flow separation.

Experimental Results

3.1. Ambient Conditions

To perform our analysis we need to first establish the ambient conditions of the wind tunnel. This section will cover the derivations of the Air Density, Dynamic Viscosity of air, Reference Dynamic Pressure, Reference Static Pressure and Reference free-stream velocity.

Air Density

To calculate the air density we can use the Ideal gas law given by equation (3.1), where M_{air} is the molecular weight of Air which we assume to be 28.97 g/mol, the atmospheric pressure is assumed to be the pressure at sea level 101325 Pa and the temperature in Kelvin is 295.55 K

$$\rho = \frac{M_{air} p_{atm}}{RT} = \frac{0.02897 \cdot 101325}{8.314462618 \cdot 295.55} = 1.19454 \text{ kg/m}^3 \tag{3.1}$$

Dynamic Viscosity of air

The dynamic viscosity of air can be calculated using Sutherland's law (3.2). Where $\mu_0 = 1.716105 kg\,m^{-1}s^{-1}$ is the the viscosity of air at a reference temperature of $T_0 = 273.15K$, and $S = 110.4K$ is the Sutherland temperature.

$$\mu = \mu_0 \left(\frac{T}{T_0}\right)^{3/2} \frac{T_0 + S}{T + S} = 1.716 \times 10^{-5} \left(\frac{295.55}{273.15}\right)^{3/2} \frac{273.15 + 110.4}{295.55 + 110.4} = 1.82478 \times 10^{-5} \text{ kg}\,\text{m}^{-1}\,\text{s}^{-1} \tag{3.2}$$

Reference Dynamic Pressure

We do not use the pitot-static tubes to measure dynamic pressure because its readings can be influenced by the presence of the model, the contraction, or the diffuser. We can find the dynamic pressure q_∞ by converting the measured pressure difference ΔP_b between the total pressure in the settling chamber and the static pressure in the contraction using a calibration curve. The calibration curve (3.3) is taken form the manual . It was generated using a pitot-static tube and mapping a correspondence between the pressure difference and dynamic pressure [3]

$$q_\infty = 0.211804 + 1.928442\,\Delta P_b + 1.879374 \times 10^{-4} \left(\Delta P_b\right)^2 \tag{3.3}$$

Reference Static Pressure

The airfoil changes the static pressure distribution in the test section, but it does not significantly affect the total pressure $p_{t,\infty}$. Therefore, we can obtain the reference static pressure from the measured total pressure and the calculated dynamic pressure q_∞ using equation (3.4), given by the manual [3].

$$p_{s,\infty} = p_{t,\infty} - q_\infty \tag{3.4}$$

Comparing this theoretical result to the value we measured , we see that..... _____ FINISH

Reference free-stream velocity

Because the flow in the tunnel is low-speed, we can treat the air as incompressible. In incompressible flow, Bernoulli (**??**)tells us that along a streamline the total pressure is the sum of static pressure and dynamic pressure.

$$p_{t,\infty} = p_{s,\infty} + \frac{1}{2}\rho U_\infty^2 \tag{3.5}$$

Substituting in equation (3.4), we receive equation (3.6)

$$q_\infty = p_{t,\infty} - p_{s,\infty} = \frac{1}{2}\rho U_\infty^2 \tag{3.6}$$

which we can rearrange to get equation (3.7) , which we can use to calculate our free stream velocity.

$$U_\infty = \sqrt{\frac{2q_\infty}{\rho}} \tag{3.7}$$

3.2. 2D Airfoil

In this section, the calculations and graphs for the 2D airfoil will be shown. At first, the flow will be analyzed and then the aerodynamic forces will be calculated and lastly, the results will be corrected.

3.2.1. Flow Near Airfoil Surface

When analyzing an airfoil, one of the most crucial coefficients is the pressure. The normal forces and the lift generated can be calculated once the difference between the upper and lower coefficients has been calculated. For this reason, the coefficient of pressure will be computed and displayed using graphs before being connected to separation and transition.

Coefficient of Pressure Calculation

In order to find the pressure coefficient (3.8) is used. P_∞ is the static pressure of the wind tunnel which is found to be 101300 Pa. In a wind tunnel test, the pressure given by the pressure tab gives the pressure relative to a reference pressure, in this scenario the pressure $P_bar = 101300$ Pa.

$$c_p = \frac{p - p_\infty}{\frac{1}{2}\rho V_\infty^2} \tag{3.8}$$

$$C_p = \frac{(P_{\text{tab}} + P_{\text{bar}}) - (P_s + P_{\text{bar}})}{\frac{1}{2}\rho V_\infty^2} = \frac{P_{\text{tab}} - P_s}{\frac{1}{2}\rho V_\infty^2} \tag{3.9}$$

V_∞ in both cases equals 18.22 m/s. This method is then repeated for every pressure tab and angle of attack. The following graphs can be calculated using the position of each tab on the upper or lower part of the airfoil. The lift force value is calculated by integrating the difference between each of the two curves.
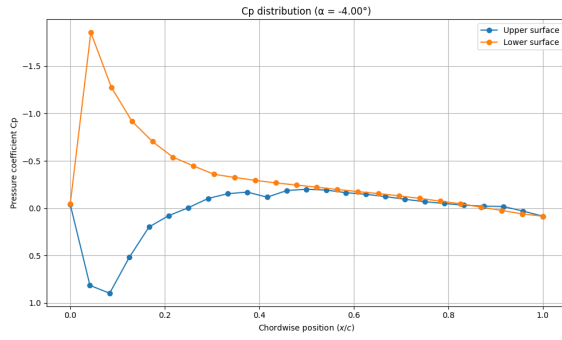
(a) C_p graph for $\alpha = -4°$
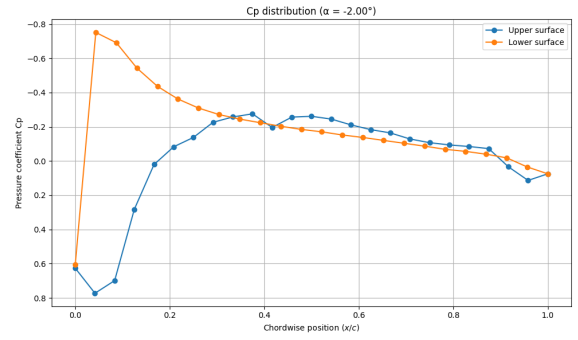
(b) C_p graph for $\alpha = -2°$
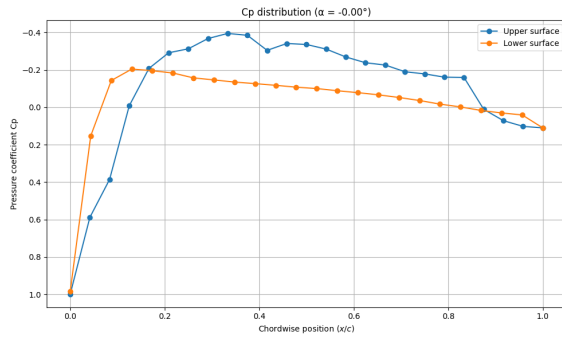
(c) C_p graph for $\alpha = 0°$
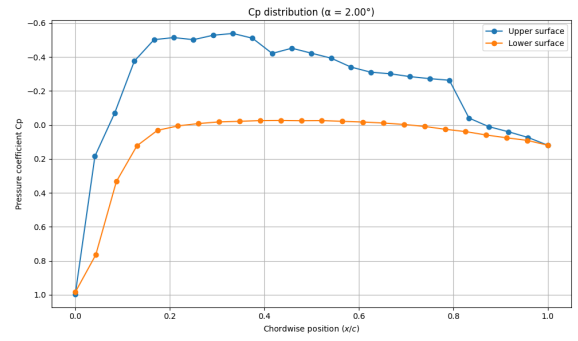
(d) C_p graph for $\alpha = 2°$
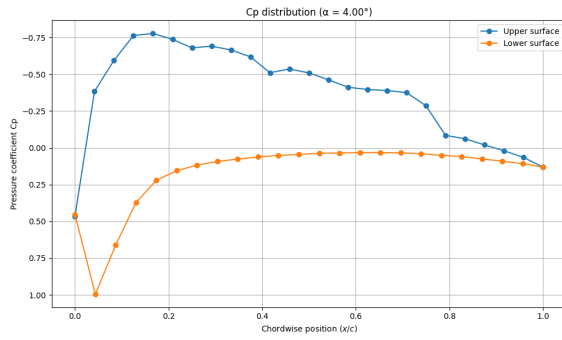
(e) C_p graph for $\alpha = 4°$
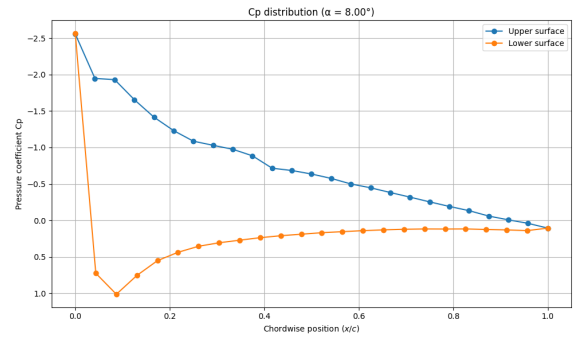
(f) C_p graph for $\alpha = 8°$
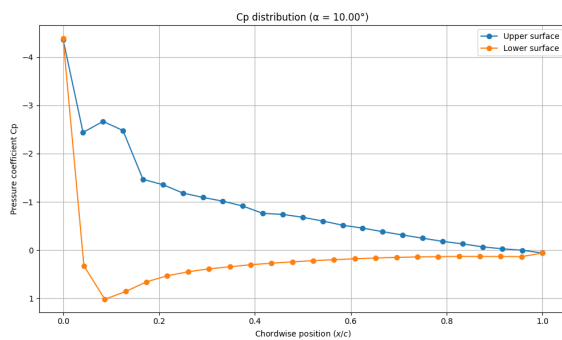
(g) C_p graph for $\alpha = 10°$
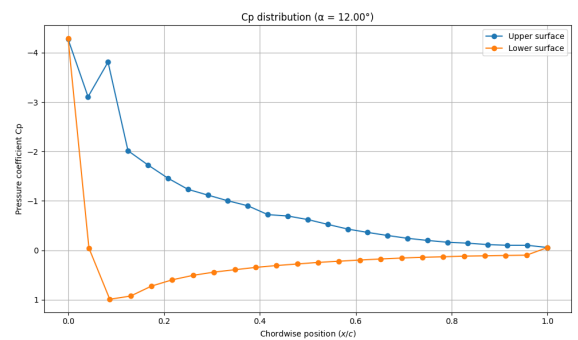
(h) C_p graph for $\alpha = 12°$
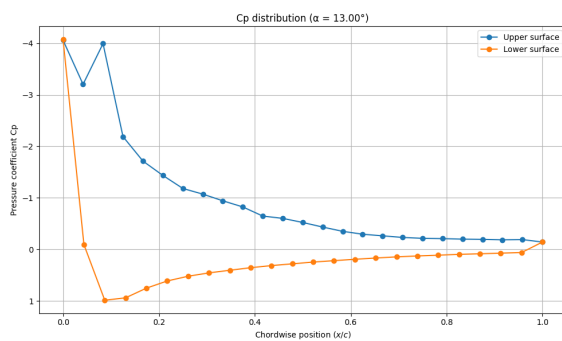
(i) C_p graph for $\alpha = 14.5°$
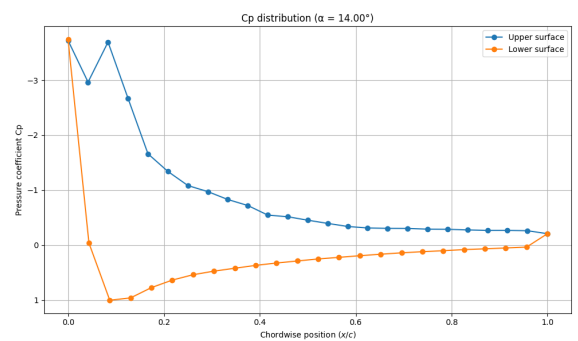
(j) C_p graph for $\alpha = 15.5°$

Figure 3.1: Combined figure of graphs of the C_p in function of chordwise position

Trend with Alpha

Looking at these results, it is evident that when α increases, so does the Cp on the upper surface of the airfoil, while the Cp of the lower surface decreases. It can be noted that the pressure difference between the upper and lower surfaces is low at an angle of attack of 0° or around it. In the graphs stall can be identified by a sharp change of the Cp profile and by an upper pressure value close to being positive.

*Transition and Separation Relation Separation and transition can be roughly identified with the Cp graph. When the pressure gradient changes to a plateau state, it is known as the separation point. On the other hand, transition happens when the plateau state returns to a sharp pressure gradient. The plateau indicates that the flow has seperated because it is no longer attached to the airfoil's surface. These behaviours can be seen in Figure 3.2, where it is visible that seperation occurs at 60% of the chord when the flow stabilses, The curve then continues to show the airfoil's shape after a transition occurs when the sharp pressure gradient becomes apparent.
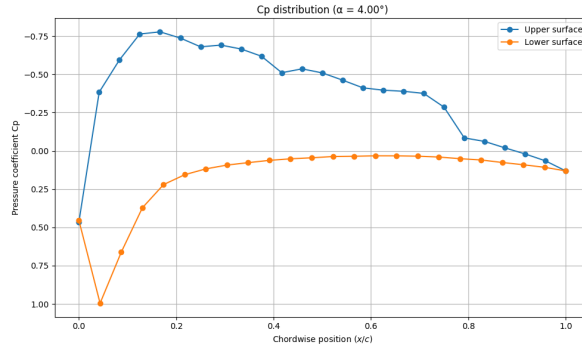

Figure 3.2: C_p curve as a function of chordwise position at $\alpha = 4°$.

3.2.2. Wake Flow Analysis

In this section the velocity profile in the wake of the airfoil will be determined based on the differences in pressures measured on the airfoil and using the wake rake. Creating this so-called wake flow velocity profile will prove very useful later on to determine the overall drag of the airfoil in section Section 3.2.5. Because the flow in this experiment is a very low-speed flow ($U_\infty = 18\,m\,s^{-1}$) the flow can be assumed to be incompressible, meaning the density will be assumed constant along the entire flow. In this experiment, the static pressure in the airfoil wake cannot be assumed to be equal to the ambient pressure due to the wake rake's proximity to the airfoil. This means Bernoulli's equation can be used to determine the velocity profile in the wake of the airfoil.

$$P_{total} = P_{static} + P_{dynamic} = P_{static} + \frac{1}{2}\rho v^2 = const. \tag{3.10}$$

This can be applied in the wake behind the airfoil, and rewritten as a function of the speed in the wake $u(y)$:

$$P_{total} = P_{static} + \frac{1}{2}\rho\,u(y)^2 \tag{3.11}$$

This equation can then be rearranged to describe $u(y)$ directly:

$$u(y) = \sqrt{\frac{2(P_{total} - P_{static})}{\rho}} \tag{3.12}$$

Unfortunately, the number of static and total pressure probes is not equal, and therefore the static and total pressures are not known at all the same locations. To solve this, the static pressure data was interpolated using a linear interpolation. Now using the python script in Appendix A, we can get the following velocity profiles for the wake of the airfoil. The python script interpolates the static pressure data from the wake rake, and then uses the result of the interpolant at the same position as the wake rake total pressure port to find the local velocity there. This is done for every total pressure port to get the velocity profiles shown in **??**:
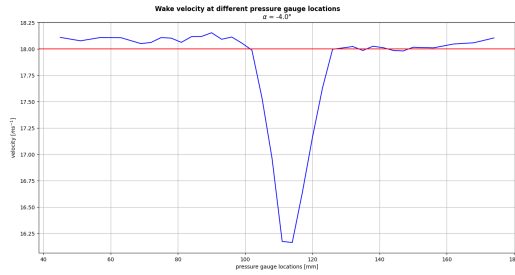
(a) velocity profile at an angle of $\alpha = -4°$
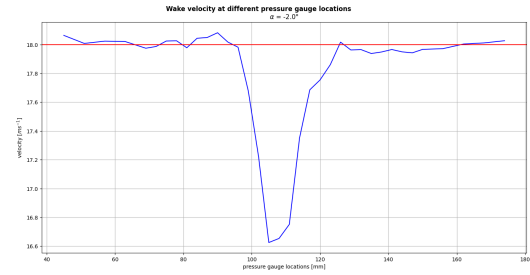
(b) velocity profile at an angle of $\alpha = -2°$
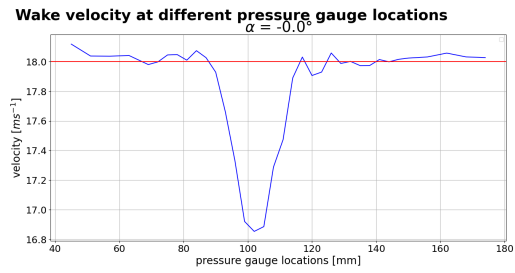
(c) velocity profile at an angle of $\alpha = 0°$
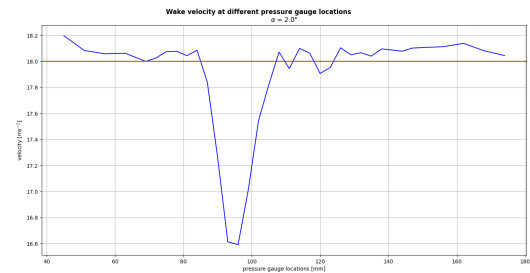
(d) velocity profile at an angle of $\alpha = 2°$

Figure 3.3: ake velocity profiles for varying angles of attack of the airfoil with respect to the freestream velocity, part 1

(a) velocity profile at an angle of $\alpha = 4°$

(b) velocity profile at an angle of $\alpha = 8°$

(c) velocity profile at an angle of $\alpha = 12°$

(d) velocity profile at an angle of $\alpha = 15°$
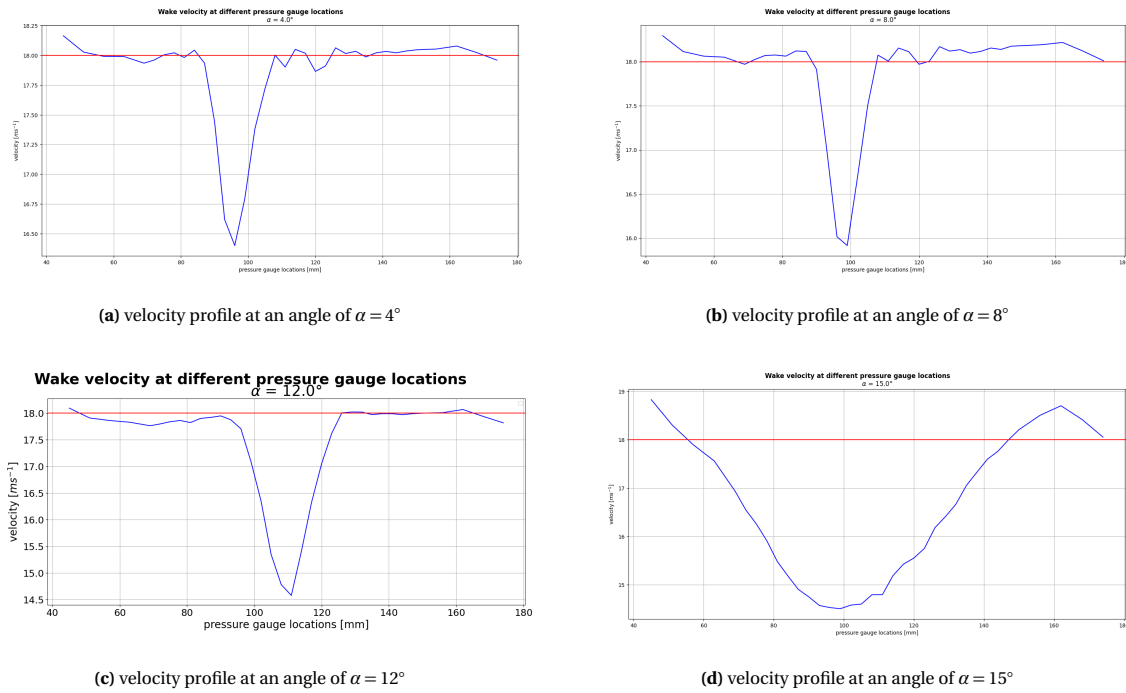
Figure 3.4: Wake velocity profiles for varying angles of attack of the airfoil with respect to the freestream velocity, part 2

The way the experiment is set up, with an airfoil wedged between a reflection plate and a turntable, means there are multiple "blockage effects" that must be taken into account, as they produce inaccuracies in the test data.

The first of these effects is the wake blockage. The result of wake blockage is the flow in the wake of the airfoil slowing down significantly, and the (relatively) undisturbed flow accelerating to a higher velocity than the freestream velocity, as can be seen in Figure 3.4 at $\alpha = 8°$.

The second effect is the solid blockage effect. This occurs due to " the result of the displacement of streamlines in the tunnel due to the volume of a non-lifting model." [4].

Both of these effects increase with increasing α, this effect can be seen very well in Figure 3.4 for $\alpha = 12°$ and $\alpha = 15°$, where it can be seen that the drop in the velocity profile widens as α increases. The drag may be overestimated due to the effective freestream velocity being higher than the velocity measured ahead of the airfoil as a result of these effects.

3.2.3. Aerodynamic Forces and Moments
The aerodynamic forces and moments acting on the airfoil can be found using the surface pressure and wake rake data obtained during the practical. Below, the methods for obtaining their respective coefficients are presented, alongside various plots and discussions of the obtained results.

Lift, Drag, and Moment from Surface Pressure Data
Finding the lift, drag, and pitching moment acting on the airfoil is a matter of integrating the pressure distribution previously discussed in this section. It is important to note that pressure drag is only one component that contributes to overall drag on the airfoil - viscous effects at the airfoil's boundary also contribute to drag, but are not accounted for at this stage. This will be discussed later on in this section. All calculations are performed using a Python tool, for which the code is presented in Appendix A.

Initially, the normal and tangential forces (N and T) in the airfoil's body reference system must be found— these are subsequently converted to lift and drag using a coordinate transformation. The coordinate systems used and the respective aerodynamic forces in their reference frames on the airfoil are depicted in Figure 3.5:
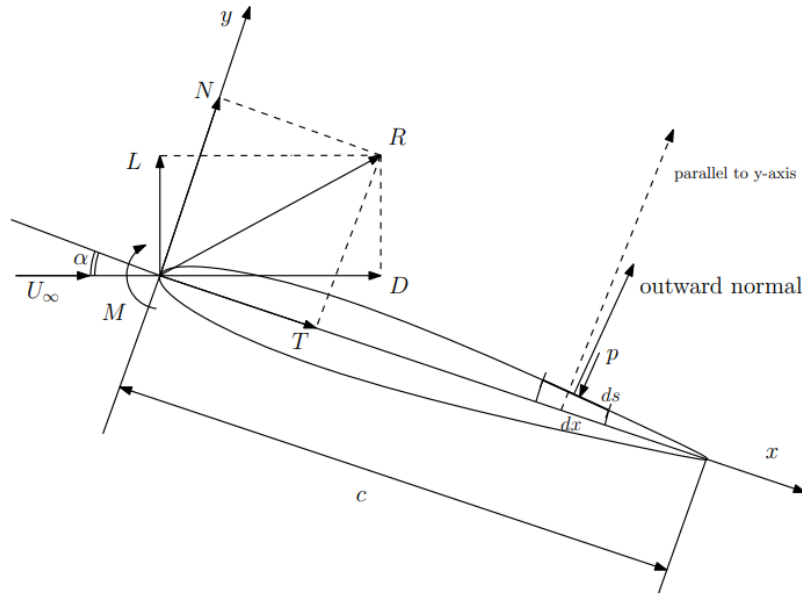
Figure 3.5: Aerodynamic and body reference frames used in relation to the airfoil *(Adapted from Veldhuis [1])*

The normal force coefficient is found using Equation (3.13) [1]:

$$c_n = \int_0^c c_{p,l} \cos\theta \, ds - \int_0^c c_{p,u} \cos\theta \, ds \tag{3.13}$$

Applying the transformation $dx = \cos\theta \, ds$ yields Equation (3.14):

$$c_n = \int_0^c c_{p,l} \, dx - \int_0^c c_{p,u} \, dx \tag{3.14}$$

Similarly, the axial force coefficient is found using Equation (3.15) [1]:

$$c_t = \int_0^c c_{p,l} \sin\theta \, ds - \int_0^c c_{p,u} \sin\theta \, ds \tag{3.15}$$

Applying the transformations $dy = \sin\theta \, ds$ and $dy = \frac{dy}{dx} dx$ yields Equation (3.16):

$$c_t = \int_0^c c_{p,l} \frac{dy}{dx} dx - \int_0^c c_{p,u} \frac{dy}{dx} dx \tag{3.16}$$

Here, $\frac{dy}{dx}$ represents the slope of the airfoil surface with respect to the chord line. This is found by interpolating the airfoil's surface coordinates, obtained from the airfoiltools website [5], and numerically approximating the derivative.

Having found the normal and tangential forces, lift and drag can be found using Equation (3.17) and Equation (3.18), respectively, in accordance with the geometry presented in Figure 3.5.

$$c_l = c_n \cos\alpha - c_t \sin\alpha \tag{3.17}$$

$$c_d = c_n \sin\alpha + c_t \cos\alpha \tag{3.18}$$

Figure 3.6 depicts the $c_l - \alpha$ and $c_l - c_d$ plots obtained using the above methods.
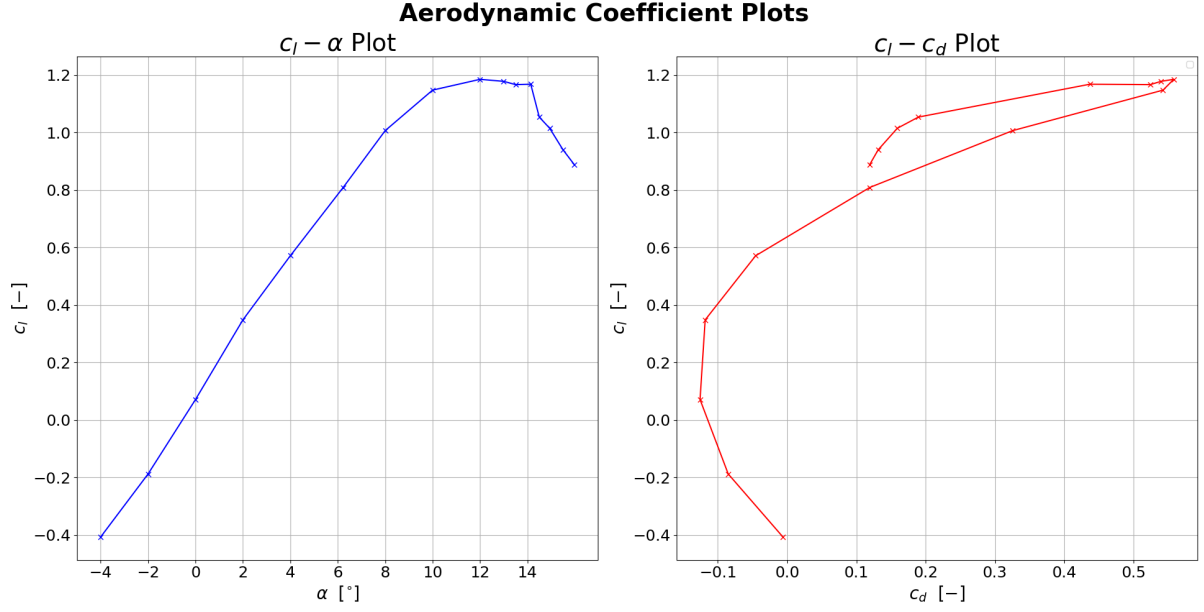
Figure 3.6: $c_l - \alpha$ and $c_l - c_d$ plots obtained from airfoil pressure data.

The lift curve depicted in Figure 3.6 behaves as expected, with a linear region for lower angles of attack, and a gradual drop in lift once stall is reached.

The drag polar is also mostly well-behaved in the linear region, while presenting erratic behavior once the airfoil reaches stall. Two aspects are noteworthy:

1. For low lift coefficient values, the drag coefficient is negative. This is caused by Equation (3.14) and Equation (3.16) neglecting viscosity and boundary layer effects: only one major component of drag in the linear region, pressure drag, is accounted for, and in conjunction with the coordinate transformation in Equation (3.18), leads to negative values for certain α.

2. Contrary to what would be expected, c_d decreases as the airfoil reaches stall. This is a consequence of the pressure distribution over the airfoil not encapsulating many of the effects that contribute to drag during stall, primarily the pressure drag created in the wake and the recirculation zones near the airfoil surface.

A more accurate estimate for c_d, taking into account viscous effects and the wake, is presented later in this report.

The leading-edge moment coefficient is found using Equation (3.19):

$$c_{m,le} = \int_0^c (c_{p,u} - c_{p,l}) x \, dx \qquad (3.19)$$

The quarter-chord moment coefficient is found from the leading-edge moment coefficient and the normal force coefficient using Equation (3.20):

$$c_{m,c/4} = c_{m,le} + \tfrac{1}{4} c_n \qquad (3.20)$$

Figure 3.7 depicts the variation of $c_{m,le}$ and $c_{m,c/4}$ with α.

(a) Leading edge moment coefficient vs. angle of attack

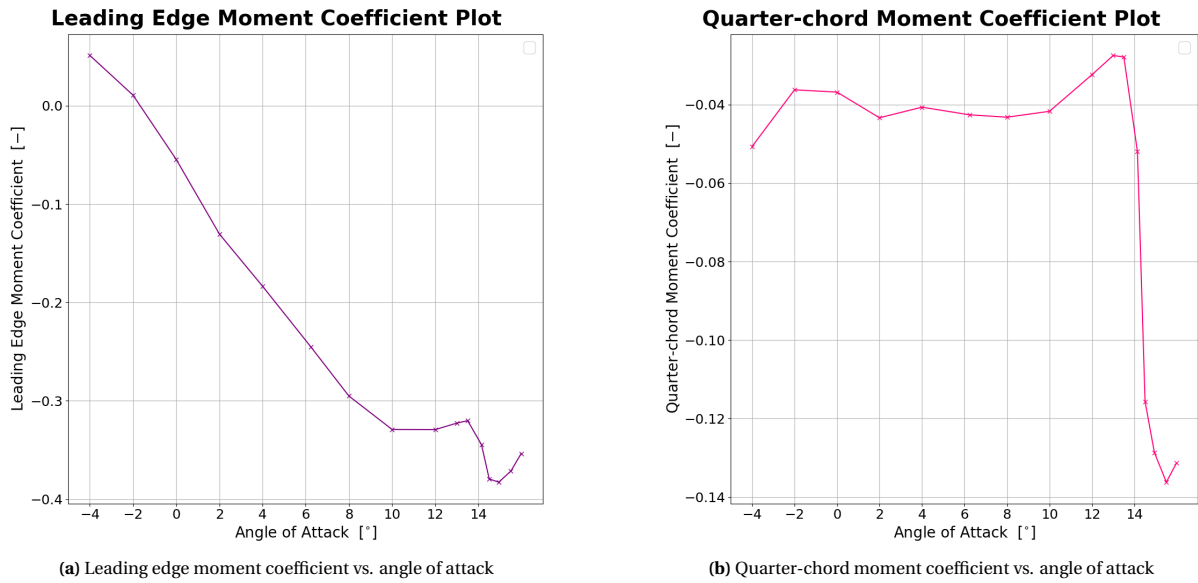**(b)** Quarter-chord moment coefficient vs. angle of attack

Figure 3.7: Airfoil pitching moment plots

The behavior of these plots are as expected. The leading-edge pitching moment of the airfoil is negative for most angles of attack, as is the slope, satisfying the requirements for aircraft stability. Upon reaching stall, the moment begins to behave somewhat erratically.

The quarter-chord moment coefficient is nearly constant for $-2° \leq \alpha \leq 10°$, with an average value of roughly -0.04. This aligns with the fact that the aerodynamic center of an airfoil, i.e. the point where $\frac{\partial c_m}{\partial \alpha} = 0$, typically sits near the quarter-chord point. Upon reaching stall, $c_{m,c/4}$ first increases, then sharply drops, reaching a value of nearly -0.14 — more than tripling the value in the linear region.

3.2.4. Center of Pressure
The center of pressure as a fraction of the chord is found using Equation (3.21):

$$\left(\frac{x}{c}\right)_{cp} = -\frac{c_{m,le}}{c_n} \tag{3.21}$$

Naturally, as c_l and $c_{m,le}$ both vary with α, the position of the center of pressure will do so as well. Figure 3.8 depicts this variance.
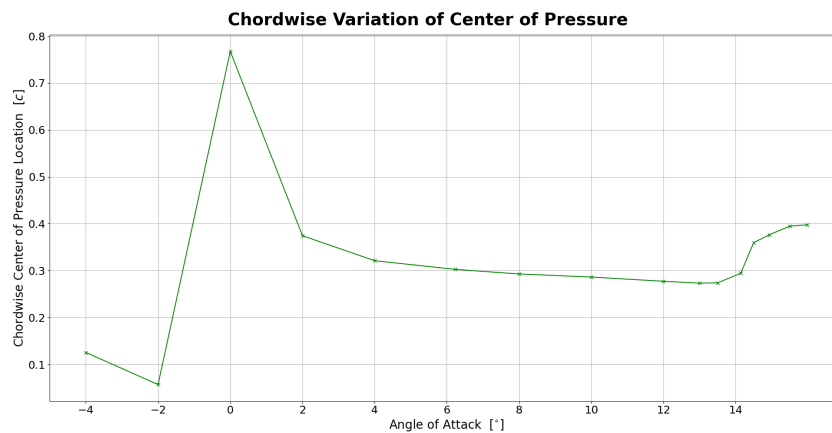

Figure 3.8: Chordwise variation of the center of pressure

For $4° \leq \alpha \leq 13.5°$, the location of the center of pressure exhibits only slight variation (moving slightly for-

ward with increasing α), averaging out to roughly $\left(\frac{x}{c}\right)_{cp} = 0.3$. From $\alpha = 13.5°$ onwards, the center of pressure moves aftwards, reaching a value of approximately $\left(\frac{x}{c}\right)_{cp} = 0.4$.

In the lower α range, the center of pressure moves substantially and erratically. At $\alpha = -4°$, the center of pressure sits rather close to the leading edge, at 12% of the chord. It moves even more forward as α increases, reaching a position of 5% of the chord at $\alpha = -2°$. At this point, as α approaches the zero-lift angle of attack $\alpha_{L=0} \approx -0.8$, the center of pressure suddenly jumps very far aftward, reaching a position of approximately 75% of the chord for $\alpha = 0°$. The shape of the graph suggests a vertical asymptote at or near $\alpha_{L=0}$ (though this has not been fully captured due to the density of data-points used). Indeed, inspecting Equation (3.21) predicts this behavior, as near $\alpha_{L=0}$, c_n will reach 0.

At first glance, it may seem physically illogical for the center of pressure to move off the airfoil in accordance with the asymptote. However, it is important to recall that the aerodynamic forces acting through the center of pressure are ultimately a mathematical representation of the distributed loads acting on the airfoil, and are thus themselves not fully physical features.

3.2.5. Drag from Wake Rake Data

In addition to integrating the pressure distribution, the airfoil's drag can be found by applying the momentum equation to a control volume surrounding the airfoil and integrating the velocity deficit measured by the wake rake. This takes into account both pressure drag and skin friction drag. Applied in this manner, the momentum equation yields Equation (3.22) [6]:

$$D = \rho \int_{wake} (u_\infty - u(y))u(y)dy - \rho \int_{wake} \overline{u'^2}dy + \int_{wake} p_\infty - p(y)dy \tag{3.22}$$

From left to right, the terms on the RHS correspond to the following:

1. Drag from mean wake velocity deficit
2. Drag from wake velocity fluctuations
3. Drag from wake pressure deficit

The test setup used in this practical was unsuitable to measure wake velocity fluctuations: thus, this term is neglected. Normalizing Equation (3.22) to obtain the drag coefficient yields Equation (3.23):

$$c_d = \frac{2}{u_\infty^2 c} \int_{wake} (u_\infty - u(y))u(y)dy + \frac{2}{\rho u_\infty^2 c} \int_{wake} p_\infty - p(y)dy \tag{3.23}$$

Figure 3.9a depicts the drag polar obtained from the wake rake data.

(a) Drag polar from wake rake data

(b) Drag polars from wake rake and surface pressure data superimposed
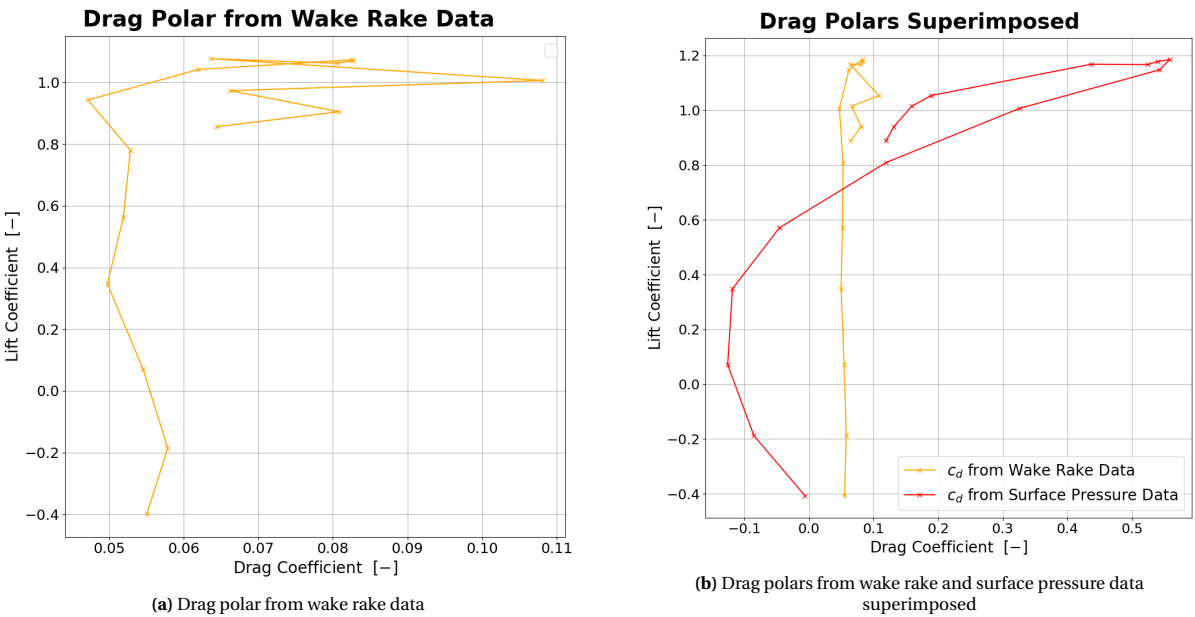
Figure 3.9: Drag polars obtained from wake rake and surface pressure data

In the linear region of the airfoil, the drag obtained from the wake rake data stays roughly constant, with an average value of roughly $c_d = 0.055$. Upon reaching stall, c_d increases markedly, reaching values more than double those in the linear range. Its behavior in the stall regime is erratic, a result of the turbulent nature of the wake in this regime.

Figure 3.9b depicts the drag polar obtained from the wake rake data superimposed on the drag polar previously obtained from surface pressure data. Clearly, the differences are significant. Whereas the wake rake c_d is roughly constant with c_l in the airfoil's linear regime, the surface pressure c_d changes roughly parabolically with c_l. As a consequence, the surface pressure c_d obtains a far wider range of values: at its minimum in the depicted range, it attains a value of $c_{d,min} \approx -0.12$, and a maximum of $c_{d,max} \approx 0.55$. These are both rather unrealistic values, as under typical flight conditions, c_d should neither be negative, nor be in the order of magnitude of 10^{-1}.

Additionally, the overall behavior of the wake rake drag polar matches the expected results far better. Most notably, c_d increases in the stall regime, whereas it decreases for the surface pressure drag polar. In the linear regime, c_d stays roughly constant — this is a desirable result for the airfoil as the airfoil's c_d will not significantly vary during normal operations.

Consequently, using the wake rake to measure the airfoil's drag is far more accurate, as its measurements are more realistic and reflect typical airfoil behavior. Neglecting viscous effects in solely considering the surface pressure acting over the airfoil introduces a significant error. Table 3.1 outlines key values from the above discussion, while Figure 3.10 depicts the error ratio of the c_d from the surface pressure data with respect to the c_d from the wake rake data.

Table 3.1: Caption

**Figure 3.10:** Caption

3.2.6. Wind Tunnel Corrections

As discussed in Section 2.5, the wall interference, wake blockage, and model blockage impact the measurements taken from the wind tunnel and therefore need to be accounted for and corrected.

3.3. 3D Wing

This section gives a closer understanding of the experimental results of the three-dimensional wing. After a first comparison with the airfoil's results, the efficiency factor and the contribution of the induced drag are estimated.

Airfoil and 3D Wing Comparison

A wing with a certain airfoil behaves differently if they are tested as finite or infinite wings. The fundamental aerodynamic forces felt by a finite and an infinite wing of the same airfoil can be seen in figure 3.11.
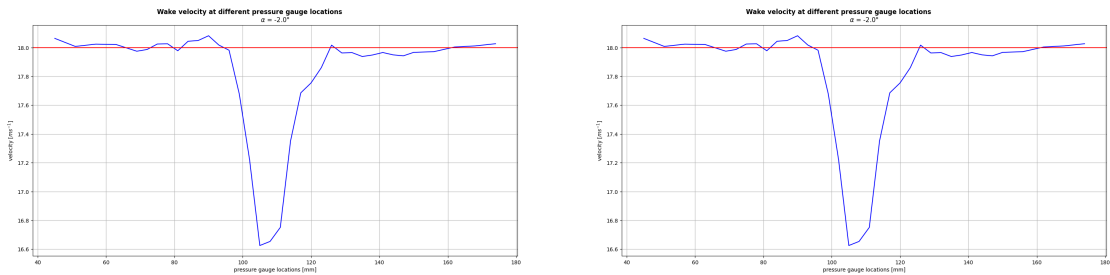
(a) Finite wing lift and drag forces at different angles of attack

(b) Infinite wing lift and drag forces at different angles of attack

Figure 3.11: Comparison of the experimental data from a finite and an infinite wing of airfoil SD6060 under similar flow conditions

placeholder figures

Induced Drag and Lift Slope Efficiency

4

Numerical Results

The numerical results from the XFOIL and XFLR5 are shown in this section, followed by a discussion comparing them with the experimental results from the wind tunnel test. The 2D aerofoil modelling in XFOIL is covered in Section 4.1, and the 3D wing analysis in XFLR5 is covered in Section 4.2.

4.1. 2D airfoil

In this section, the results obtained in the experiment using the 2D airfoil will be compared to the results obtained using the XFOIL simulation. This section aims to evaluate and explain the differences between the results of the simulation and those gathered in the experiment. Analysis using XFOIL requires two basic parameters to start with, the Reynolds number and the Mach number. During the experiment the Reynolds number was noted to be around 190.000, which was entered into XFOIL. The Mach number can be found using the following equation:

$$M = \frac{v}{\sqrt{\gamma R T}} \tag{4.1}$$

Here γ (the heat capacity ratio) is known to be 1.4, R (the universal gas constant) is known to be $287 \frac{J}{kg \cdot K}$. Furthermore v (airstream velocity) was measured to be $18 m s^{-1}$ during the experiment. Lastly standard sea-level conditions were assumed regarding T (temperature) to be $288.15 K$. This allowed the freestream Mach number to be calculated as 0.0529.
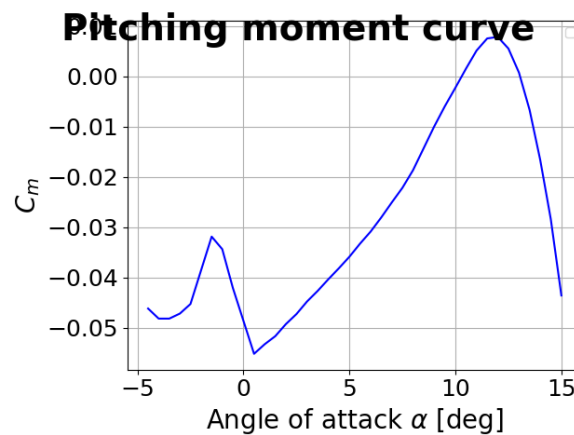
4.1.1. Comparison of Aerodynamic Forces
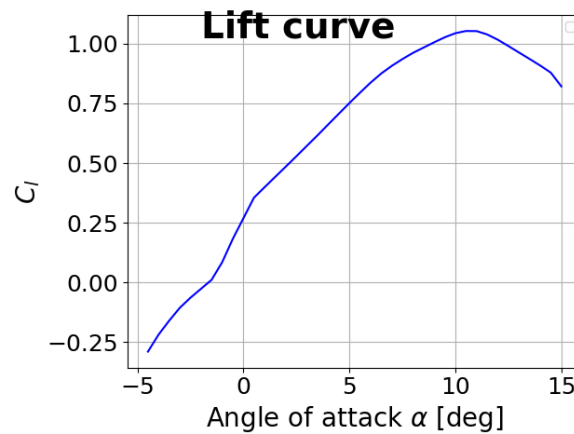
(a) Lift curve obtained using XFOIL
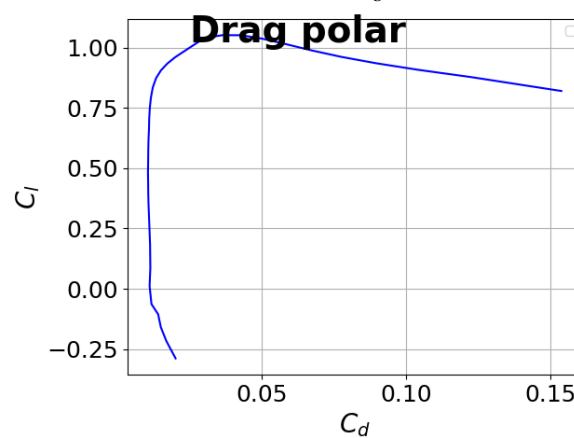
(b) Drag polar obtained using XFOIL

(c) Pitching moment curve obtained using XFOIL

Comparison of Pressure Distribution

When looking at the upper surface pressure, it is clear that the XFOIL overestimates the pressure coefficients close to the leading and trailing edges of the airfoil at $\alpha = -4°$, this may indicate that there is a local seperation. Looking at the lower surface, there are small variations which may be happening by the laminar bubble behaviour that the XFOIL is not able to replicate accurately. Overall, in this AoA, the XFOIL provides

Curves should follow curve conventions

a good model for the pressure coefficients.

Figure 4.2: Pressure coefficient distribution obtained from XFOIL and experimental data at $-4°$.

ADD FIG-UREEEEE

Now, observing Figure 4.3, the pressure coefficients at 4° are shown. Comparing the upper surfaces reveals that the XFOIL overestimates the initial pressure spike at the leading edge and continues to overpredict the pressure coefficient up to 40% of the chord. The XFOIL shows a sharper pressure drop at around 60% chord than the experimental data which can be a result of a miss prediction of the laminar bubble size. Analysing the aerofoil's lower surface the XFOIL overestimates the pressure coefficients throughout the chord, resulting in higher C_l values.

Figure 4.3: Pressure coefficient distribution obtained from XFOIL and experimental data at $\alpha = 4°$.

ADD FIG-UREEEEE

Finally, the distribution of pressure coefficients at 10° is shown in Figure 4.4. The pressure coefficient over the upper surface shows a strong initial spike that quickly decreases in both numerical and experimental results; however, XFOIL takes longer to decrease than the experimental results. Further down the chord on the upper surface, XFOIL predicts pressure coefficients that align well with the experimental data. The lower surface of the aerofoil shows that XFOIL typically follows the shape of the experimental curve; however, it consistently overpredicts the pressure coefficients.

Figure 4.4: Pressure coefficient distribution obtained from XFOIL and experimental data at $\alpha = 10°$.

ADD FIG-UREEEEE

4.2. 3D finite Wing

In this section, the results from the XFLR5 simulation and experiments are compared. The comparison will first focus on the aerodynamic forces and then on the induced drag and efficiency values.

XFLR5 Setup

To have very accurate and comparable results to the measurements, the simulation in XFLR5 was set up based on values learned from the experiment. The first step of the simulation was to analyse the 2D airfoil with XFOIL at 5 different Reynolds numbers, as this ensures that the data for the finite wing converges as much as possible. Since the experiment was performed at a Reynolds number of $1.9 \cdot 10^5$, the airfoils polars were plotted at Reynolds numbers of $1.3 \cdot 10^5$, $1.7 \cdot 10^5$, $1.9 \cdot 10^5$, $2.1 \cdot 10^5$, and $2.5 \cdot 10^5$. The air density is also assumed to be 1.91kg/m^3, the average of the measurements of the finite wing experiment.

To adapt the 2D results to a 3D wing, a mesh of the finite wing, like in !!!ADD SKETCH!!! , also with an SD6060 airfoil, is created. In the simulation, it is assumed that the experiment is only half of what its full wingspan would be. That way, when later only half the simulated wing, therefore only one wingtip vortice, is taken into account, while the other end doesn't have any wingtip interference. Additionally, the wing tips rounding at the leading edge is approximated.

As explained in section 2.6, LLT, VLM1, VLM2, and 3D Panels can be used to simulate the finite wing. As VLM1 and VLM2 barely differ from one another, only VLM2 was excluded from the simulations. The three simulation methods used, namely LLT, VLM1, and 3D panels, are used to compare the aerodynamic coefficients experienced over the entire wing as well as the induced drag distributed over the wing span.

Aerodynamic Forces Comparison

Both computed and measured aerodynamic coefficients for the finite wing are plotted in !!!!!ADD GRAPH!!!!!. The first graph shows the lift curve, and the right graph is a representation of the drag polar. The simulation method or results are specified in the legend of the graph.

ADD EVALUATION OF BEST SUITED SIMULATION METHOD

Induced Drag

5

Discussion

Bibliography

[1] Veldhuis, L., "Manual for Low Speed Windtunnel Test AE2130-II," WebPage, 2025. URL `https://brightspace.tudelft.nl/d2l/le/content/782577/viewContent/4437047/View`, date Accessed: 20/12/2025.

[2] XFLR5 Development Team, "Guidelines for XFLR5 V4.07," Tech. rep., XFLR5, Jul. 2008. User guidelines.

[3] *AE2130-II Wind Tunnel Practical Manual (v1.6)*, Delft University of Technology, 2025. Course manual, provided to students.

[4] Bernhard Stoevesandt, P. F. Y. S., Gerard Schepers, *Handbook of Wind Energy Aerodynamics*, Springer, 2020.

[5] n.d., "Airfoil Tools | SD6060-104-88," WebPage, 2025. URL `http://airfoiltools.com/airfoil/details?airfoil=sd6060-il`, Date accessed: 19/12/2025.

[6] Kotsonis, M., "AE2130-II: Low-speed wind tunnel test Instructions for lab report," WebPage, 2025. URL `https://brightspace.tudelft.nl/d2l/le/content/782577/viewContent/4437047/View`, date Accessed: 20/12/2025.

A
Python Code

```
1
2  placeholder
3
```